A new tropospheric tomography model combining the pixel-based and function-based models

Yibin Yao [1,2,*], **Linyang Xin** [1] **and Qingzhi Zhao** [3]

[1] School of Geodesy and Geomatics, Wuhan University, Wuhan 430079, China;
    ybyao@whu.edu.cn (Y.Y); linyangxin@whu.edu.cn (L.X);

[2] Key Laboratory of Geospace Environment and Geodesy, Ministry of Education, Wuhan University, Wuhan 430079, China

[3] College of Geomatics, Xi'an University of Science and Technology, Xi'an 710054, China;
    zhaoqingzhia@163.com

*   Correspondence: ybyao@whu.edu.cn; Tel.: +86-027-68758401

Abstract:As a new detection method of three-dimensional water vapor, the ground-based water vapor tomography technique using Global Navigation Satellite Systems (GNSS) observations can obtain the high spatial and temporal distribution information of tropospheric water vapor. Since the troposphere tomography was proposed, most previous studies belong to the pixel-based method, dividing the interest area into three-dimensional voxels of which the water vapor density of each voxel center is taken as the average water vapor density. However, the abovementioned method can only find the water vapor density value of the center of each voxel, which is unable to express the continuous change of water vapor in space and destroys the spatial continuity of water vapor variation. Moreover, when using the pixel-based method, too many voxels are needed to express the water vapor density, which leads to the problem of too many coefficients to be estimated. After analyzing the limitations of the traditional pixel-based troposphere tomography technique, this paper proposes a new GNSS tropospheric water vapor tomography model combining the pixel-based and function-based models for the first time. The tomographic experiences were validated using the data from 12 stations from the Hong Kong Satellite Positioning Reference Station Network (SatRef) collected between 25 March and 25 April 2014. The comparison between tomographic results and the European Centre for Medium-Range Weather Forecasts (ECMWF) data is mainly used to analyze the accuracy of the new model proposed in this paper under different conditions, for showing that this new model is superior to the traditional pixel-based model in terms of root-mean-square error (RMSE) and bias. The new model has more advantages than the traditional pixel-based model on the RMSE, especially when obtaining the water vapor in voxels without the penetration of GNSS rays, which is improved by 5.88%. This model also solves the problem with more ease and convenience in expression.

Keywords:GNSS;water vapor tomography; functional-based technique; ECMWF

1. Introduction

The distribution of water vapor is complex and highly variable, and water vapor, as the most active key component of the atmosphere, is indeed hard to describe accurately (Rocken et al., 1997). An in-depth understanding of temporal and spatial variation of water vapor plays an important role in improving the accuracy of weather forecasting and early warning of disastrous weather (Weckwerth et al., 2004).

GNSS water vapor monitoring techniques can not only acquire the two-dimensional spatial and temporal distribution of water vapor in the horizontal direction (Bevis et al, 1994; Emardson et al, 1998; Baltink et al, 2002; Bock et al, 2005) but can also use a three-dimensional tomography method to reconstruct the vertical structure of water vapor at high temporal-spatial resolution (Flores et al, 2000; Seko et al, 2000; Macdonald et al, 2002).

Braun et al. (1999) first proposed the concept of reconstructing the tropospheric water vapor structure using 20 GPS stations in a regional observational network. Flores et al. (2000) first presented a method of recovering slant wet delay (SWD) and obtained the water vapor density using the observation of SWD by singular value decomposition (SVD) combined with a least square method. In the same year, Hirahara (2000) used different methods to conduct tropospheric tomography experiments, which also confirmed the feasibility of obtaining three-dimensional water vapor fields using GPS technology. Since then, many scholars have studied GNSS troposphere tomography techniques and completed many research experiments (Rohm et al, 2014; Yao Y B et al., 2016a, 2016b, 2016c).

Regarding the tropospheric tomographic model solution and algorithm improvement, Hirahara et al. (2000) conducted a four-dimensional tropospheric wet refractivity retrieval of the GPS network from Shigaraki and solved the observation equations using the damping least-squares method, which is commonly used in seismic tomography. Braun et al. (2003, 2004) overcame the sensitivity problem in tomographic results by using the extended sequential filtering method. Perler et al. (2011) presented a new parameterization method for water vapor retrieval. The measured and simulated data proved that this method can obtain better tomographic solution results of water vapor. Adavi and Mashhadi (2015) used virtual reference station observations to retrieve the three-dimension distribution of atmospheric water vapor information in northwestern Iran. The results showed that this method can effectively improve the rank deficit problem of the tomographic normal equation. Nilsson and Gradinarsky (2006) obtained the tropospheric tomographic results directly from the original GNSS phase observations combined with the Kalman filter method. Rohm and Bosy (2009) used the Moore-Penrose pseudo-inverse of variance-covariance to solve the linear equations and emphasized the ill-posed tomography equation. Zhao and Yao (2016) also obtained good results by using the optimal grid-making method for water vapor tomography. In the meantime, a method of using the side-penetrating signals for tomography was proposed to improve the effect of GNSS ray utilization rate.

Although GNSS tomography techniques have been developed for more than two decades, it has been challenging to enhance the water vapor quality and the stability of the solution results through the multi-system and multi-source data combination method and improve the tomographic model solution and algorithm. However, in the previous studies, most water vapor tomography methods belong to the pixel-based model, which means that the three-dimensional meshes of the study area were used, and the water vapor density at the center of each voxel was taken as the average water vapor density of the whole voxel. However, only could find the water vapor density value of the center of each voxel, the pixel-based tomography is unable to continuously express the change of water vapor in space and also breaks the spatial continuity of the water vapor. Since the three-dimensional water vapor density is stored through the voxels, a large amount of voxel information (spatial position, water vapor density within the voxel, etc.) is required

81   when describing the spatial water vapor density distribution, which is inconvenient for later use (Yao Y,

82   Chen P, 2013). What's more, though some constraints could be put on apriori models in order to overcome

83   the ill-posed problem in pixel-based tomography, some errors due to empirical constraints would be added

84   artificially. Thus, this paper analyzes the limitations of traditional pixel-based tropospheric water vapor

85   tomography and proposes a new tropospheric tomography model combining the pixel-based and function-

86   based models. This method combines the advantages of both the function-based method in facilitating the

87   continuity of water vapor expression in spatial-temporal distribution and the pixel-based method ease in

88   solving to retrieve the three-dimensional water vapor distribution in the interest region. The experimental

89   results show that the accuracy of the new combinatorial model is improved, and the new model has more

90   advantages when obtaining the water vapor in voxels without GNSS rays penetrating. Under strong rainfall

91   weather conditions, the tomographic results of the new combinatorial model are more stable and reliable.

92

93   **2. A tropospheric tomography model combining the pixel-based and function-based models**

94   *2.1. Establishment of the traditional troposphere tomography model*

95   2.1.1. Retrieval of SWV

96   For tropospheric tomography, the most important observation is the slant water vapor (SWV), which

97   is related to the water vapor density and can be defined by

98    $$SWV = \int_S \rho_V ds \quad (1)$$

99   where s represents the path of the satellite signal ray, and ρ_V is the water vapor density (units: g/m³).

100   SWV can be obtained by the following method:

101   $$SWV = \frac{10^6}{R_\omega [(k_3 / T_m) + k_2']} \cdot SWD \quad (2)$$

102   where k_2' =16.48 K hPa⁻¹, k₃=3.776×10⁵ K² hPa⁻¹, and R_ω =461(J kg⁻¹ K⁻¹), which represent the specific

103   gas constants for water vapor. T_m is the weighted mean tropospheric temperature, calculated from an

104   empirical equation proposed by Liu et al. (2001) using the meteorological measurements. SWD is the slant

105   wet delay, which may be given as

106   $$SWD_{elv,\varphi} = m_{wet}(elv) \times ZWD + m_{wet}(elv) \times \cot(elv) \times (G_{NS}^w \times \cos\varphi + G_{WE}^w \times \sin\varphi) + R \quad (3)$$

107   where elv is the satellite elevation, φ is the azimuth, m_{wet} is the wet mapping function, G_{NS}^w and G_{WE}^w

108   are the wet delay gradient parameters in the east–west and north–south directions, respectively. R refers to

109   the unmodeled zero difference residuals that may involve unmodeled influnce on three-dimensional spatial

110   water vapor distribution, which can make up for the lack of tropospheric anisotropy using only the gradient

111   term (Bi et al. 2006). Since the GAMIT software only provide the double difference residuals, the zero

112   difference residuals in this paper are obtained from the double difference residuals according to the method

113   proposed by Alber et al. (2000). ZWD is the zenith wet delay, which is extracted from the zenith

114   tropospheric delay (ZTD) by separating the zenith hydrostatic delay (ZHD) using equation ZWD=ZTD-

115   ZHD. ZHD can be calculated precisely using surface pressure based on the Saastamoinen model

116   (Saastamoinen 1972):

117
$$ZHD = \frac{0.002277 \times P_s}{1 - 0.00266 \times \cos(2\varphi) - 0.00028 \times H} \quad (4)$$

118 where P_s is the surface pressure (unit: hPa), φ is the latitude of the station, and H is the geodetic

119 height (unit: km). The unit of ZHD is meter.

120   Since the SWV is obtained, the tomographic area can be discretized into a number of voxels, in which

121 water vapor density is a constant during a given period of time. Therefore, a linear equation relating SWV

122 and water vapor density can be established as follows (Chen and Liu 2014):

123

124
$$SWV^p = \sum_{ijk}(D_{ijk}^p \bullet \rho_{ijk}) \quad (5)$$

125 where SWV^p is the slant water vapor of ρ th signal path (unit: mm). i, j, and k are the positions of

126 discrete tomographic voxels in the longitudinal, latitudinal and vertical directions, respectively. D_{ijk}^p is

127 the distance of the ρ th signal in voxel (i, j, k) (unit: km). ρ_{ijk} is the water vapor density in a given voxel

128 (i, j, k) (unit: g/m^3). A matrix form of this observation equation can be rewritten as follows (Flores et al.

129 2000; Chen and Liu 2014):

130
$$y_{m \times 1} = A_{m \times n} \bullet \rho_{n \times 1} \quad (6)$$

131 where m is the number of total SWVs, and n is the number of voxels in the tomographic area. y is the

132 observed value here as the SWV, which penetrates the whole interest area, A is the coefficient matrix of the

133 signal transit distances through the voxels, and ρ is the column vector of the unknown water vapor

134 density.

135 2.1.2. Constraint equations of the Tomography Modeling

136   Solving for the unknown water vapor density in Eq. (6) is actually an inversion algorithm issue as the

137 design matrix A is a large sparse matrix, whose normal equation is singular, leading to numerical problems

138 when using a direct inversion method (Bender et al., 2011a). To overcome this rank deficiency problem,

139 constraint equations are often introduced to the tomography equation (Flores et al., 2000; Troller et al.,

140 2002; Rohm and Bosy, 2009; Bender et al., 2011a). In our study, horizontal constraint equation is imposed

141 by the Gauss-weighted functional method (Guo et al, 2016) and the vertical constraint equation is imposed

142 by the functional relationship of the exponential distribution (Cao Y, 2012), respectively. The final

143 tomography model is then obtained as

144
$$\begin{pmatrix} A_{m \times n} \\ H_{m \times n} \\ V_{m \times n} \end{pmatrix} \bullet \rho_{n \times 1} = \begin{pmatrix} y_{m \times n} \\ 0_{m \times n} \\ 0_{m \times n} \end{pmatrix} \quad (7)$$

145 where H and V are the coefficient matrices of horizontal and vertical constrains, respectively. In order to

146 obtain the inverse matrix shown in Eq. (7), singular value decomposition is used in this paper (Flores et al.,

147 2000).

148 *2.2. Tropospheric tomography model combining the pixel-based and function-based models*

149   The combinatorial tomographic model proposed in this paper can take full advantage of the function-

based model in facilitating the continuity of water vapor expression in spatial-temporal distribution and the
pixel-based model in calculating water vapor density conveniently. The combinatorial tomographic model
begins to obtain the water vapor density saved as the observation value from voxels penetrated by GNSS
rays using the traditional pixel-based tomographic model and then obtains the optimal polynomial function
of each layer through adaptive training. Using the optimal polynomial fitting function of each layer with
known coefficients, the water vapor densities can finally be calculated in any tomographic region by given
the latitude, longitude and the altitude. Specific steps are as follows:

First, use the traditional pixel-based tomography model to obtain the initial water vapor density from
voxels penetrated by GNSS rays in the tomographic region of each layer as the observed values for
obtaining the optimal polynomial function coefficient of each layer.

Second, normalize the coordinates of each voxel center in the tomographic area. Since the polynomial
fitting of the water vapor at each tomographic layer is in essence establishing the relationship between the
latitude as well as the longitude of the tomographic region and the water vapor density. The general
expression is:

$$V_d = a_0 + a_1 B + a_2 L + a_3 BL + a_4 B^2 + a_5 L^2 + a_6 B^2 L \cdots \quad (8)$$

where B is the latitude, L is the longitude, and V_d represents the water vapor density. Polynomial

coefficients such as a_i are obtained via the least squares method. In the process of solving, because the
numerical values of latitude and longitude are not small, the magnitude of multiple power may be larger
than 10^4, which will lead to the ill-posed problem of the design matrix in the inversion process and affect
the reliability of the estimated coefficients. To ensure that the design matrix constructed will be relatively
stable in the inversion process, the latitude and longitude coordinates B and L need to be normalized. The
specific methods are as follows:

$$B^* = \frac{B - \mu_B}{\sigma_B}$$

$$L^* = \frac{L - \mu_L}{\sigma_L} \quad (9)$$

where B^* and L^* are the normalized latitude and longitude, respectively, and B and L are the

latitude and longitude in the initial region range. μ is the average value of latitude or longitude, and σ
is the standard deviation of latitude or longitude.

Third, build the function-based model part of the new combinatorial tomographic method, through
adaptive training to determine the optimal polynomial function of each layer.

- First, based on the size of the selected tomographic region, determine the highest
  polynomial fit order. In this paper, the highest polynomial fit order chosen as 5 turns out to
  be generally sufficient.
- Through obtaining the water vapor density from voxels penetrated by GNSS signal rays in
  the tomographic region of each layer as the input value and constantly trying out new
  polynomial functions, the optimal polynomial function of each layer is obtained by
  simulated training.

  During the processes of training and comparison, the number of voxels penetrated by GNSS

186   rays initially should be paid attention to since the number of estimated coefficients need to

187   be less than that of the voxels penetrated by GNSS rays in each layer. Under this premise,

188   the over-fitting problem should also be avoided, otherwise it would be counterproductive.

189   •   Finally, after comparison of the training results of multi-group polynomial functions at

190   different levels, the polynomial function of the minimum RMSE value after the post-fitting

191   layer and fitting of the ECMWF results is the best fit equation for this layer. Each layer

192   could have the individual optimal polynomial function in general.

193   Fourth, after finding the optimal polynomial function of each layer in different heights, use the latitude,

194   longitude and altitude information into the function to obtain the three-dimensional water vapor distribution

195   of any position in the tomographic region. The three-dimensional water vapor field in the tomographic zone

196   can be described by broadcasting the estimated coefficients of the optimal polynomial function of each

197   layer.

198   *2.3. The optimal polynomial selection based on adaptive training*

199   Since the polynomial form can better reflect the continuity of water vapor and has the advantage of

200   high-efficiency computing as well as easy expression, this paper chooses the polynomial form as the

201   function-based model. The selection process of the optimal polynomial function based on adaptive training

202   is as follows:

203   First, to construct a polynomial equations training library, which contains a wide variety of polynomial

204   function forms of latitude and longitude as independent variables, use the water vapor density in the voxels

205   as the dependent variable. After many experiments, the maximum power of latitude and longitude found as

206   5 is sufficient to describe the water vapor changes. Therefore, the maximum power of the function-base

207   part is adopted as 5 in the training library.

208   Second, according to the water vapor density observations from the voxels penetrated by the GNSS

209   signals at each level, the form of the candidate polynomial function of each layer is automatically

210   determined from the polynomial function training library to ensure that the number of observations at all

211   levels is always greater than the number of estimated coefficients of the candidate polynomials.

212   Third, calculate the water vapor variation index (WVVI) of each layer in both east-west and south-

213   north directions with the traditional tropospheric tomographic results as shown in Eq. (10).

214

$$WVVI = \frac{\overline{\nabla wv_{EW}}}{\overline{\nabla wv_{NS}}} \qquad (10)$$

215   Where wv_{EW} and wv_{NS} are the water vapor density in east-west and south-north direction, separately.

216   The WVVI, a changing rate indicator of water vapor density in a given direction, is obtained by

217   calculating the overall average change rate of water vapor density in a given direction within each adjacent

218   voxel. According to the water vapor variation index of each layer in the east-west and north-south direction,

219   it can be determined whether water vapor exists mainly in the east-west distribution or the north-south

220   distribution. As an aid, WVVI can choose the main body of the alternative polynomial function with higher

221   order term of longitude or latitude for the subsequent accuracy comparison in order to efficiently and

222   quickly find the optimal polynomial function of each layer. If the water vapor density of a layer indicates a

223   horizontal gradient of east-west distribution, the polynomial function with higher-order term of longitude

224   should be given the priority. It suggests that when the water vapor shows an east-west gradient distribution

225   there is a better correlation between longitude and water vapor variation, furthermore the high-order term

226   in longitude can better reflect the nuanced water vapor variation. A simple example of the polynomial

227 function with a higher-order term in longitude is shown in Eq. (11):

$$V_d = a_0 + a_1 B + a_2 L + a_3 BL + a_4 L^2 + a_5 BL^2 + a_6 L^3 \qquad (11)$$

229 Otherwise, when the water vapor density of a layer indicates a horizontal gradient of north-west
230 distribution, the polynomial function with higher-order term of latitude should be given the priority. A
231 simple example is shown in Eq. (12):

$$V_d = a_0 + a_1 B + a_2 L + a_3 BL + a_4 B^2 + a_5 B^2 L + a_6 B^3 \qquad (12)$$

233 While the distribution regularities of water vapor density gradient are not clear and obvious, the
234 polynomial function with the same order of latitude and longitude can be considered as the example shown
235 in Eq. (13):

$$V_d = a_0 + a_1 B + a_2 L + a_3 BL + a_4 B^2 + a_5 L^2 \qquad (13)$$

237 Fourth, the candidate polynomials of all levels screened by the WVVI gradient auxiliary information
238 are used as the next comparative polynomials, and the required estimated coefficients of the comparative
239 polynomial are solved according to the principle of least squares through Eq. (14) and automatically
240 recorded into the coefficients data set. M is the matrix of longitude and latitude, and the vector x comprises
241 the unknown coefficients of the comparative polynomial functions as shown in Eq. (15).

$$V_d = Mx \qquad (14)$$

$$x = \begin{bmatrix} a_0 \\ a_1 \\ \vdots \\ a_n \end{bmatrix} \qquad (15)$$

244 Fifth, through the comparative polynomials with the estimated coefficients in each layer, the whole-
245 voxel water vapor fitting of each layer is automatically fit with the information of the latitude and longitude.
246 In order to obtain the RMSE, the fitting result would be compared with the ECMWF water vapor density
247 of each layer in this period. The results are then saved to the accuracy data sets of each layer. The
248 comparative polynomials with the estimated coefficients are constantly selected to train the fitting of the
249 layered water vapor density and then compared with the water vapor density of ECMWF at each layer.
250 Thus, large accuracy data sets of RMSE can be obtained, where the smallest RMSE value of the
251 comparative polynomial form can be chosen, and then the optimal polynomial of each layer could come
252 into being. It is noteworthy that the optimal polynomial of each layer might be different. With the optimal
253 polynomial of each layer, the three-dimensional water vapor density in the tomographic region can be
254 expressed conveniently and continuously by transmitting the estimated coefficients information.

255 **3. Experiment**

256 *3.1. Experimental description and data-processing strategy*

257 To study whether the accuracy and stability of the results of the tropospheric tomography model
258 combining the pixel-based and function-based models proposed in this paper are better than the traditional
259 pixel-based tropospheric tomography model, the following experiment is designed.

260 Tomographic data is obtained from the SatRef Network for Hong Kong from 25 March 2014 to 25
261 April 2014. Two epochs are taken each day (0:00 and 12:00). The corresponding meteorological data is
262 also used to calculate the PWV. The tomographic area ranges between latitude 22.23°N to 22.53°N and

263 longitude 113.87°E to 114.29°E. Taking the mean sea level as the height of base level, the vertical resolution

264 is 0.8 km, and total grid number is 5 × 7 × 13. In the selected area, a total of 11 GNSS stations and 1

265 radiosonde station are selected, and the ECMWF grid data are extracted twice daily at UTC 00:00 and 12:00

266 from 25 March 2014 to 25 April 2014 (grid resolution of 0.125 × 0.125). See Fig. 1 for details.

267

268
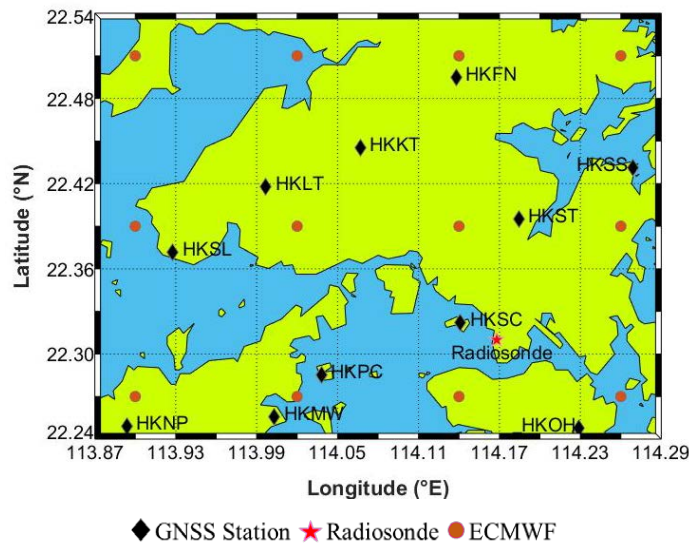
269 **Figure 1: The GNSS (11 black rhombuses) and radiosonde (1 red star) stations and ECMWF comparative points**

270 **(12 ochre circles) in Hong Kong. The grid lines display tomography grids.**

271 According to the official website of the Hong Kong Observatory

272 (http://www.weather.gov.hk/contentc.htm) for the weather review, Hong Kong had a total of 15 days of

273 rainy weather during 25 March 2014 to 25 April 2014, as shown in Table 1.

274

Table 1. Rainfall information for March and April 2014

Date	Rainfall situation
3.29	Thunderstorms turn to heavy rain
3.30	Thunderstorms turn to heavy rain
3.31	Thunderstorms turn to heavy rain
4.1	Shower accompanied by wind, thunderstorms
4.2	Showers, reports of hail in some areas
4.3	Showers, some parts of the rain are quite large
4.6	Cloudy shower, low temperature
4.7	Heavy shower, low temperature
4.8	Showers, low temperatures
4.14	Shower
4.21	Cloudy turns to the shower
4.22	Showers and foggy
4.23	Showers turn to the rain
4.24	Showers turn to the cloudy
4.25	Cloudy turns to the rain

275 In this paper, GAMIT (v10.50) (Herring et al., 2010) software was used for processing the GPS

276   observations based on the double-differenced model at a sampling interval of 30 s, and the global mapping

277   function was adopted. The zenith total delay (ZTD) and wet horizontal gradient intervals were estimated at

278   0.5 h and 2 h, respectively. Based on the surface pressure obtained from observed meteorological

279   parameters, the ZHD could be obtained by the Saastamoinen model, and ZWD was isolated from ZHD.

280   Via GMF projection, the SWD could be obtained by transforming the observed SWV.

281   *3.2. Experimental introduction and program comparison*

282   The RMSE and bias of the combinatorial tomographic model residuals were calculated by subtracting

283   the ECMWF water vapor density from the water vapor density of the GNSS tropospheric tomography

284   model combining the pixel-based and function-based models (hereinafter referred to as combinatorial

285   tomographic model). In a similar way, the RMSE and bias of the traditional tomographic model residuals

286   can also be obtained from the difference between the ECMWF water vapor density and the three-

287   dimensional water vapor density obtained by the traditional ground-based GNSS pixel-based troposphere

288   water vapor tomography model (hereinafter referred to as the traditional tomographic model).

289   In the period of data processing, the situation can be compared on a case-by-case basis to

290   comprehensively evaluate the accuracy of the combinatorial tomographic model from various views. In this

291   paper, 6 case scenarios are investigated, comprising the spatial distribution scenario, the everyday

292   distribution scenario, the rainy situation and the non-rainy case. Moreover the residuals of water vapor

293   density in voxels with and without penetrating GNSS rays are inspected. The definitions of 6 case scenarios

294   abovementioned are as follows:

295   The spatial distribution scenario is investigated by obtaining the RMSE and bias of the residuals from

296   all ECMWF comparative points at all time intervals as well as the accuracy of each layer in thirteen layers

297   of the tomographic area is calculated.

298   The everyday distribution situation is found by obtaining the RMSE and bias of the residuals from all

299   ECMWF comparative points in two epochs each day, and the overall accuracy of 32 days between 25 March

300   and 25 April, 2014 was calculated.

301   The rainy case is based on the distribution of 15 days of rainy days between 25 March and 25 April,

302   2014, as referred to in Table 1, in which the RMSE and bias of the residuals are obtained from all ECMWF

303   comparative points in all the epochs in rainy days for further accuracy analysis. Similarly, the non-rainy

304   situation is found with an accuracy analysis of the non-rainy days.

305   The situation of residuals of water vapor density in voxels without GNSS rays penetration is found by

306   obtaining the RMSE and bias of the residuals from ECMWF comparative points without rays passing

307   through in all the epochs each day. Conversely, the situation with GNSS rays penetration is found by

308   obtaining the RMSE and bias of the residuals from ECMWF comparative points with rays passing through

309   in all the epochs each day.

310   According to the above classifications, the accuracy of the combinatorial tomographic model residuals

311   and the traditional tomographic model residuals were calculated, and the accuracy of the new model was

312   compared with the traditional model to determine which model is better.

313   **4. Interpretation of the results**

314   *4.1. Accuracy information of the spatial distribution situation*

315   To verify whether the accuracy of the combinatorial tomographic model is better than that of the

316   traditional tomographic model, the layered RMSE and bias of the residuals from all ECMWF comparative

317   points at all time intervals between the tomography (using both the optimal polynomial function of each

318   layer and the traditional way) and the ECMWF results are obtained and shown in Table 2, and the

319   calculation of RMSE improvement percentage involved in the following tables is shown in Eq. (16).

$$\Delta RMS\% = \left(RMS_{trad} - RMS_{comb} \right) / RMS_{trad} \cdot 100\% \quad (16)$$

where $RMSE_{comb}$ is the RMSE value of the residuals calculated from the combinatorial tomographic

model, and $RMSE_{trad}$ is the RMSE value of the residual obtained from the traditional tomographic

model.

Table 2 shows that RMSE and bias values obtained by the combinatorial tomographic model are
smaller than those of the traditional tomographic model, and the RMSE improvement percentage is positive,
which indicates that the combinatorial tomographic model has a higher accuracy than the traditional
tomographic model overall. Moreover, the RMSE improvement percentage is appreciable in the upper
region because the value of water vapor density in high altitude is very small, even the small changes in the
upper region could result in a large percentage change. In addition, the bias and RMSE in the bottom from
Table 2 are not as good as those of the other higher layers, regardless of which model is used. These results
could be mainly ascribed to a certain system deviation between the comparison data of ECMWF and the
GNSS tomographic data. Besides, the observations and the number of redundant observations are
insufficient due to less rays passing through the voxels in the bottom and then result in low accuracy. What's
more, the water vapor content in the bottom region too abundant and changeable to be generally describe
accurately. The above reasons lead to large bias and RMSE in the bottom tropospheric area.

Table 2. Statistics of two models' tomography accuracy with respect to ECMWF data in the spatial
distribution scenario in 2014 (Unit: g/m³)

Layer	bias		RMSE		RMS Improvement Percentage
	Traditional model	Combinatorial model	Traditional model	Combinatorial model	
1	-7.81	-7.65	8.17	8.00	2.06%
2	-3.52	-3.42	3.95	3.83	3.14%
3	-0.90	-0.80	1.66	1.60	4.05%
4	0.72	0.61	1.39	1.36	2.00%
5	1.62	1.58	1.87	1.83	2.28%
6	1.95	1.77	2.10	2.09	0.39%
7	1.98	1.90	2.25	2.20	2.07%
8	1.76	1.68	2.15	2.10	2.32%
9	1.62	1.60	2.06	2.04	1.10%
10	1.34	1.11	1.85	1.47	20.68%
11	1.04	0.87	1.60	1.25	21.75%
12	0.74	0.61	1.26	0.96	23.67%
13	0.44	0.38	0.71	0.58	18.36%

4.2. The accuracy information of the everyday distribution situation

To determine whether the accuracy of the combinatorial tomographic model is better than that of the
traditional tomographic model on the everyday time scale, the RMSE improvement percentage is obtained
from all ECMWF comparative points (a total of 12) at two epochs each day using both the optimal
polynomial function of each layer and the traditional method. Figure 2 shows that the percentage of RMSE
improvement per day is practically positive, and the percentage of April 11th can even approach 12%,
indicating that the improvement seems to be appreciable. This improvement shows that the accuracy of the

345   combinatorial tomographic model is mostly superior to that of the traditional tomographic model in
346   everyday distribution; however, on April 7, April 9 and April 15, the RMSE improvement percentage is
347   negative. This might be due to the heavy showers bringing rapid water vapor change from April 7 to April
348   8 and on April 14, which is difficult to fit the polynomial function well with the unstable water vapor.
349   However, since negative percentages do not exceed -1%, the accuracy of these four days calculated by the
350   combinatorial tomographic model could be considered basically equivalent to that of the traditional
351   tomographic model.

352
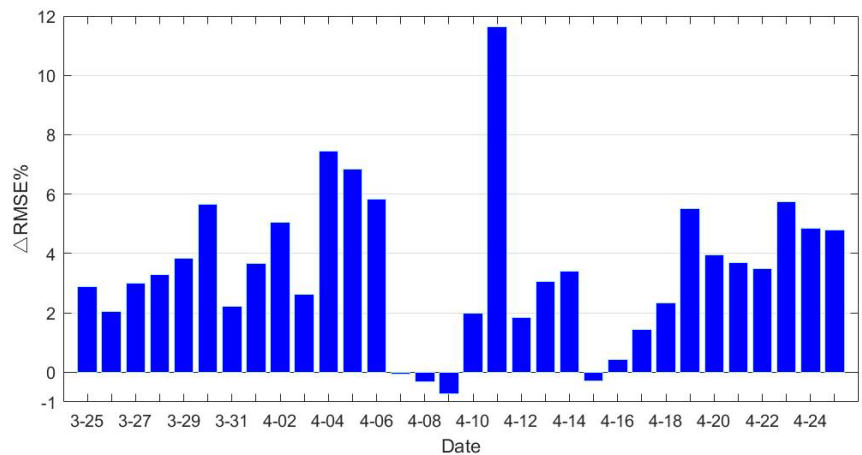
353   **Figure 2: Everyday Distribution Statistics of Daily RMSE Improvement Percentage between 25 March and 25**
354   **April, 2014.**

355   In addition, the overall RMSE and bias of the residuals are obtained from the ECMWF comparative
356   points (a total of 12) in two epochs under the entire everyday distribution situation. The statistical results
357   are shown in Table 3 below.

358   **Table 3.** Statistics of two models' tomography accuracy with respect to ECMWF data in the everyday
359   distribution scenario in 2014 (Unit: g/m^3)

Statistics type	Traditional model	Combinatorial model	RMS improvement percentage
RMS	2.97	2.87	3.44%
bias	0.07	0.02	

360   Table 3 shows that the RMSE obtained by the combinatorial model is smaller by 3.44% compared to
361   the traditional one. The combinatorial model bias more closes to zero, indicating that the combinatorial
362   tomographic model has better stability and less systematic deviation from the comparative data. Taking the
363   extreme weather conditions such as the heavy rainfall during the period into account, the accuracy of the
364   combinatorial tomographic model seems to be higher in bad weather situations to a certain extent.
365   Compared with the traditional tomographic model, the new model can obtain a certain improvement in the
366   tomographic results of water vapor density.

367   *4.3. The accuracy information of rainy and non-rainy situations*

368   To further analyze the reliability of the combinatorial tomographic model compared with the
369   traditional tomographic model in different weather conditions, according to the distribution of rainy days
370   in Table 1, all the rainy days data and non-rainy days data are used separately for tomography to obtain the

371 RMSE and bias of the residuals under corresponding weather conditions. The number of matching points

372 is still 12 (see Fig. 1). The overall statistical results are shown in Table 4.

373 **Table 4.** Statistics of two models' tomography accuracy with respect to ECMWF data in the rainy

374 situation and the non-rainy case in 2014 (Unit: g/m³)

(a) The overall rainy situation statistics			
Statistics type	Traditional model	Combinatorial model	RMS improvement percentage
RMS	3.05	2.94	3.68%
bias	0.05	-0.01	
(b) The overall non-rainy situation statistics			
Statistics type	Traditional model	Combinatorial model	RMS improvement percentage
RMS	2.89	2.80	3.21%
bias	0.10	0.04	

375 Table 4 (a) shows that the RMSE and bias of the residuals calculated by the combinatorial tomographic

376 model are better than those of the traditional tomographic model using rainy day data. The RMSE of the

377 combinatorial tomographic model is 3.68% higher than the traditional model, indicating the accuracy of

378 the new model is superior. The combinatorial model bias closes more to zero than the traditional one, which

379 means the new model has an increase in stability and a reduction in the system error. Using non-rainy day

380 data, the RMSE and bias of the residuals calculated by the combinatorial tomographic model are also better

381 than those of the traditional tomographic model, see Table 4 (b). The RMSE improvement percentage is

382 3.21%, also indicating there is an improvement in the accuracy of the new model. Besides, the

383 combinatorial model bias is more close to zero, making the system error weakened and the stability

384 enhanced. According to the RMSE improvement percentage under the rainy and non-rainy situations, the

385 RMS improvement percentage of rainy days is better than that of non-rainy days. This finding shows that

386 the combinatorial tomographic model is more suitable for obtaining the tomographic results when severe

387 water vapor changes occur.

388 *4.4. The accuracy information of voxels with and without GNSS rays penetrating situations*

389 In the traditional pixel-based water vapor tomographic model, the water vapor density in the voxels

390 without GNSS rays passing through depends on the accuracy of the water vapor density in the adjacent

391 voxels with GNSS rays penetration. However, the combinatorial tomographic model uses an optimal

392 polynomial as the function-based model for overall fitting to obtain the water vapor density in voxels

393 without penetrating GNSS rays. To determine whether the function-based model part of the combinatorial

394 method contributes better to the accuracy of water vapor density in voxels without GNSS rays passing

395 through, the situations of voxels with and without GNSS rays penetration as described in section 3.2 were

396 designed. After obtaining the RMSE and bias of the residuals using the combinatorial and traditional

397 tomographic models separately under designed situations, the overall accuracy information of voxels with

398 and without GNSS rays penetrating shows in Table 5.

399

Table 5. Statistics of two models' tomography accuracy with respect to ECMWF data in the voxels with and without penetrating GNSS rays in 2014 (Unit: g/m³)

(a) The overall situation statistics of voxels without rays penetrating			
Statistics type	Traditional model	Combinatorial model	RMS Improvement Percentage
RMS	3.40	3.20	5.88%
Bias	1.59	1.51	
(b) The overall situation statistics of voxels with rays penetrating			
Statistics type	Traditional model	Combinatorial model	RMS Improvement Percentage
RMS	3.27	3.24	1.00%
bias	1.70	1.65	

Table 5 (a) shows that the RMSE and bias of the residuals calculated by the combinatorial tomographic model are better than those of the traditional tomographic model in the situation of voxels without GNSS rays penetrating. Moreover the RMSE of combinatorial tomographic model is 5.88% better than that of the traditional tomographic model, and the bias decreased from 1.59 to 1.51. To a certain extent, this finding shows that the combinatorial tomographic model is more advantageous for obtaining the water vapor density from the voxels without GNSS rays penetrating, which is consistent with the initial hypothesis: the traditional tomographic model uses constraint equations in section 2.1.2, Eq. (7), which is unable to well represent the distribution of water vapor density from voxels without GNSS rays penetrating in the actual situation. However, the new proposed model uses the exact water vapor density from voxels with GNSS rays penetrating as the observation value for further fitting the water vapor density in voxels without GNSS rays penetrating, using optimal polynomial functions with estimated coefficients established by relatively actual water vapor distribution in each layer. In comparison, the combinatorial tomographic model can better reflect the layered actual situation of continuous water vapor changes, and the accuracy is naturally better. What's more, the RMSE and bias obtained by the combinatorial tomographic model are also superior to those of the traditional tomographic models using the classified data of voxels with GNSS rays penetrating, see Table 5 (b). The RMSE calculated by the new model is 1% higher than the traditional model, and the bias reduced by 4.73% from 1.7 to 1.65. In summary, whether it is calculated separately from data of voxels with or without GNSS rays penetrating, the results of the combinatorial tomographic model are superior to those of the traditional tomographic model to a certain extent, which could prove the advanced nature and reliability of the combinatorial tomography model.

In order to double-check if the combinatorial tomography model in the situation of voxels without GNSS rays passing through shows a better result in the vertical distribution of 3D water vapor density, the water vapor density profiles for different altitudes at individual times are given in Fig. 3. Two times (0:00 UTC 11 April 2014 and 12:00 UTC 11 April 2014) are chosen for they correspond to the maximum percentage of RMSE improvement during the experiment period of 32 days. Figure 3 shows that in the situation of voxels without GNSS rays penetration, the water vapor profile of combinatorial tomography model better matches that from ECMWF than the traditional tomographic model at both times, especially in the bottom layers, which implies that the water vapor density derived from the proposed model is superior to that of the traditional tomography model in the situation of voxels without penetrating GNSS rays.

431
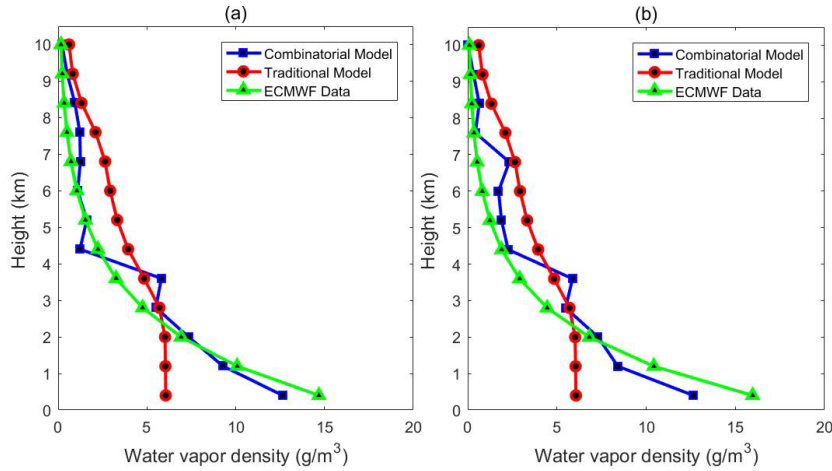
Figure 3: Water vapor profiles derived from ECWMF and two models in the situation of voxels without
penetrating GNSS rays, (a) and (b) are periods of 0:00 – 0:30 UTC 11 April 2014 and 12:00 – 12:30 11 April
2014, respectively.

Furthermore, to compare directly the vertical accuracy of water vapor density derived from different
altitudes in the situation of voxels without penetrating GNSS rays, the tomographic results (25 March 2014
to 25 April 2014) from two different tomography models are analyzed. Figure 4 shows the percentage of
RMSE improvement and relative error change with altitudes. The percentage of RMSE improvement in
Fig. 4 is defined as the same as Eq. (16), and the relative error is defined by using the Eq. (17).

$$RE = \frac{\rho - \rho_{ECMWF}}{\rho_{ECMWF}} \qquad (17)$$

where RE is the relative error, ρ represents the water vapor density derived from the traditional or
combinatorial tomography model, and ρ_{ECMWF} is the water vapor density derived from ECMWF grid
data.

It can be observed in Fig. 4 that in the situation of voxels without GNSS rays penetration, the
percentage of RMSE improvement is positive in lower layers while negative in some middle and upper
layers, which could prove that the proposed model improves the accuracy of tomography results in most
layers when there are seldom voxels with GNSS rays penetrating especially in the bottom layers. Due to
the lack of GNSS observation data, the bottom accuracy of tomographic results is always low. In addition,
Figure 4 shows in the situation of voxels without GNSS rays penetration, the relative error begins to
decrease with the altitude and then increases above 3 km. When the altitude is higher, the relative error
becomes larger, this is due to the small water vapor values of the upper layers, and just a very tiny difference
could cause a large relative error between the models and ECMWF water vapor density data.
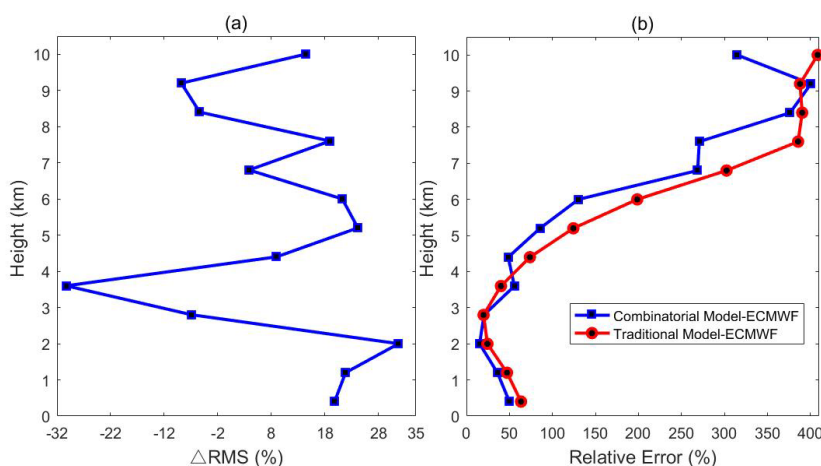
Figure 4: The percentage of RMSE improvement and relative error change with height in the situation of voxels without GNSS rays penetration (blue curve and red curve are derived from the differences between the profiles of the combinatorial tomography model, the traditional tomographic model and ECMWF grid data, separately for 64 epochs spanning from 25 March 2014 to 25 April 2014).

5. Conclusion

In this paper, a new tropospheric tomography model combining the pixel-based and function-based models has been proposed, which is much more concise and convenient in expression and use than the traditional pixel-based tomographic model. Only the optimal polynomial coefficients of each layer as the function-based part are required to describe the three-dimensional water vapor distribution in the tomographic region. By using the SatRef GNSS network observation data in Hong Kong between 25 March and 25 April, 2014, the RMSE and bias have been assessed in 6 scenarios. The situations include the spatial distribution situation and the everyday distribution situation, the rainy situation and the non-rainy situation, and the voxels with and without GNSS rays penetrating situations. The results demonstrate that regardless of the situation, the RMSE and bias of the new combinatorial tomographic model are better compared to the traditional tomographic model. Among these situations, when there are voxels without GNSS rays penetrating, the RMSE improvement percentage can be significantly increased up to 5.88%, which shows that the combinatorial tomographic model is more advantageous for obtaining the water vapor density from voxels without GNSS rays passing through. For the rainy situation, the bias improvement percentage can reach 76.18%, which shows that the proposed model is more stable in heavy rainfall. However, some shortcomings remain in the GNSS tropospheric combinatorial tomographic model. For example, when constructing the optimal polynomial of each layer, the polynomial is not only limited by the water vapor density quality in voxels with rays passing through calculated by the traditional pixel-based tomographic model, but it is also limited by the size of the tomographic area and the situation of dividing voxels. In the future, the purely function-based tomographic model of the troposphere should be further studied, which is free from the above limitations. It is expected that the tropospheric tomographic model will be more conveniently used and expressed when the polynomial coefficients could be obtained directly from SWVs.

Acknowledgments: The authors would like to thank ECMWF for providing access to the layered meteorological data. The Lands Department of HKSAR is also acknowledge for providing GPS data from the Hong Kong Satellite Positioning Reference Station Network (SatRef) and corresponding meteorological data.

Conflicts of Interest: The authors declare that they have no conflict of interest.

485 **References**

486 Adavi Z, Mashhadi-Hossainali M. 4D-tomographic reconstruction of water vapor using the hybrid
487 regularization technique with application to the North West of Iran. Adv. Space Res. 2015, 55, 1845-1854.

488 Alber C, Ware R, Rocken C, et al. Obtaining single path phase delays from GPS double differences.
489 Geophys. Res. Lett. 2000, 27, 2661–2664.

490 Baltink H K, Marel H V D, Hoeven A G A V D. Integrated atmospheric water vapor estimates from a
491 regional GPS network. J Geophys Res-Atmos, 2002, 107, ACL 3-1–ACL 3-8.

492 Bender M, Stosius R, Zus F, et al. GNSS water vapour tomography – Expected improvements by combining
493 GPS, GLONASS and Galileo observations. Adv. Space Res. 2011, 47, 886-897.

494 Bevis M, Businger S, Chiswell S R, et al. GPS meteorology: mapping zenith wet delays onto precipitable
495 water. J Appl Meteor, 1994, 33, 379-386.

496 Bi Y, Mao J, Li C. Preliminary results of 4D water vapor tomography in the troposphere using GPS. Adv
497 Atmos Sci, 2006, 23:551–560.

498 Bock O, Keil C, Richard E, et al. Validation of precipitable water from ECMWF model analyses with GPS
499 and radiosonde data during the MAP SOP. Q J Roy Meteor Soc, 2005, 131, 3013-3036.

500 Braun J J. Remote sensing of atmospheric water vapor with the global positioning system. Geophys. Res.
501 Lett. 2004, 20, 2631-2634.

502 Braun J, Rocken C, Meertens C, et al. Development of a Water Vapor Tomography System Using Low Cost
503 L1 GPS Receivers. Proc, 1999.

504 Braun J. Comparisons of line-of-sight water vapor observations using the global positioning system and a
505 pointing microwave radiometer. J Atmos Ocean Tech, 2003, 20, 606-612.

506 Cao, Y. GPS Tomographying Three-Dimensional Atmospheric Water Vapor and Its Meteorological
507 Applications. Ph.D. Thesis, The Chinese Academy of Sciences, Beijing, China, 2012

508 Chen B, Liu Z. Voxel-optimized regional water vapor tomography and comparison with radiosonde and
509 numerical weather model. J Geodesy, 2014, 88, 691-703.

510 Emardson T R, Elgered G, Johansson J M, et al. Three months of continuous monitoring of atmospheric
511 water vapor with a network of Global Positioning System receivers. J Geophys Res, 1998, 103, 1807-1820.

512 Flores A N, Ruffini G, Rius A, et al. 4D tropospheric tomography using GPS slant wet delays. Ann Geophys
513 Ger, 2000, 18, 223-234.

514 Guo J, Yang F, Shi J, et al. An Optimal Weighting Method of Global Positioning System (GPS) Troposphere
515 Tomography, IEEE J-STARS,2016, PP(99):1-8.

516 Herring, T. A., King, R. W., & McClusky, S. C. Documentation of the GAMIT GPS Analysis Software
517 release 10.4. Department of Earth and Planetary Sciences, Massachusetts Institute of Technology,
518 Cambridge, Massachusetts. 2010.

519 Hirahara K. Local GPS tropospheric tomography. Earth Planets Space, 2000, 52, 935-939.

520 Liu YX, Chen YQ, Liu JN. Determination of weighed mean tropospheric temperature using ground
521 meteorological measurements. Geospatial Inf Sci, 2001, 4, 14-18.

522 Macdonald A E, Xie Y, Ware R, et al. Diagnosis of Three-Dimensional Water Vapor Using a GPS Network.
523 Mon Weather Rev, 2002, 130, 386-397.

524 Nilsson T, Gradinarsky L. Water vapor tomography using GPS phase observations: simulation results. IEEE
525 T Geosci Remote, 2006, 44, 2927-2941.

526 Perler D, Geiger A, Hurter F. 4D GPS water vapor tomography: new parameterized approaches. J Geodesy,
527 2011, 85, 539-550.

528 Rocken C, Van Hove T, Ware R, et al. Near real‐time GPS sensing of atmospheric water vapor. Geophys.

529   Res. Lett. 1997, 24, 3221-3224.

530   Rohm W, Bosy J. Local tomography troposphere model over mountains area. Atmos Res, 2009, 93, 777-
531   783.

532   Rohm W, Zhang K, Bosy J. Limited constraint, robust Kalman filtering for GNSS troposphere tomography.
533   Atmos Meas Tech, 2014, 6, 1475-1486.

534   Saastamoinen J. Atmospheric Correction for the Troposphere and Stratosphere in Radio Ranging Satellites.
535   Use of Artificial Satellites for Geodesy, 1972, 15, 247-251.

536   Seko H, Shimada S, Nakamura H, et al. Three-dimensional distribution of water vapor estimated from
537   tropospheric delay of GPS data in a mesoscale precipitation system of the Baiu front. Earth Planets Space,
538   2000, 52, 927-933.

539   Troller M, Bürki B, Cocard M, et al. 3-D refractivity field from GPS double difference tomography.
540   Geophys. Res. Lett. 2002, 29, 2-1–2-4.

541   Weckwerth T M, Parsons D B, Koch S E, et al. An overview of the international H2O project (IHOP_2002)
542   and some preliminary highlights. B Am Meteorol Soc, 2004, 85, 253-277.

543   Yao Y B, Zhao Q, Zhang B, et al. A method to improve the utilization of GNSS observation for water vapor
544   tomography. Ann. Geophys. 2016, 34, 143-152.

545   Yao Y, Chen P, Zhang S, et al. A new ionospheric tomography model combining pixel-based and function-
546   based models. Adv. Space Res. 2013, 52, 614-621.

547   Yao Y, Zhao Q. A novel, optimized approach of voxel division for water vapor tomography. Meteorol
548   Atmos Phys, 2017, 129, 1-14.

549   Yao Y, Zhao Q. Maximally Using GPS Observation for Water Vapor Tomography. IEEE T Geosci Remote,
550   2016, 54, 7185-7196.

551   Zhao Q, Yao Y. An improved troposphere tomographic approach considering the signals coming from the
552   side face of the tomographic area. Ann. Geophys. 2017, 35, 87-95.